JGR Space Physics

RESEARCH ARTICLE
10.1029/2021JA029337

The Roles of the Magnetopause and Plasmapause in Storm-Time ULF Wave Power Enhancements

J. K. Sandhu[1], I. J. Rae[1], F. A. Staples[2], D. P. Hartley[3], M.-T. Walach[4], T. Elsden[5], and K. R. Murphy[6]

[1]Department of Mathematics, Physics, and Electrical Engineering, Northumbria University, Newcastle upon Tyne, UK, [2]Mullard Space Science Laboratory, University College London, London, UK, [3]Department of Physics and Astronomy, University of Iowa, Iowa City, IA, USA, [4]Department of Physics, Lancaster University, Lancaster, UK, [5]School of Physics and Astronomy, University of Leicester, Leicester, UK, [6]Thunderbay, ON, Canada

This article is a companion to Sandhu et al. (2021), https://doi.org/10.1029/2020JA028423.

Key Points:

- Ultra low frequencies (ULF) wave power is enhanced across a wide range of dayside L values during storms
- The magnetopause position is a dominant variable in the radial dependence of ULF wave power
- Plasmaspheric plumes are associated with spatially localized enhanced ULF wave power

Supporting Information:

Supporting Information may be found in the online version of this article.

Correspondence to:

J. K. Sandhu,
jasmine.k.sandhu@northumbria.ac.uk

Citation:

Sandhu, J. K., Rae, I. J., Staples, F. A., Hartley, D. P., Walach, M.-T., Elsden, T., & Murphy, K. R. (2021). The roles of the magnetopause and plasmapause in storm-time ULF wave power enhancements. *Journal of Geophysical Research: Space Physics*, *126*, e2021JA029337. https://doi.org/10.1029/2021JA029337

Received 17 MAR 2021
Accepted 15 JUN 2021

Abstract Ultra low frequency (ULF) waves play a crucial role in transporting and coupling energy within the magnetosphere. During geomagnetic storms, dayside magnetospheric ULF wave power is highly variable with strong enhancements that are dominated by elevated solar wind driving. However, the radial distribution of ULF wave power is complex - controlled interdependently by external solar wind driving and the internal magnetospheric structuring. We conducted a statistical analysis of observed storm-time ULF wave power from the Van Allen Probes spacecraft within 2012–2016. Focusing on the dayside (06 < magnetic local time ≤ 15), we observe large enhancements across $3 < L < 6$ and a steep L dependence during the main phase. We consider how accounting for concurrent magnetopause and plasmapause locations may reduce statistical variability and improve parameterization of spatial trends over and above using the L value. Ordering storm time ULF wave power by L provides the weakest dependences from those considered, whereas ordering by distance from the magnetopause is more effective. We also explore dependences on local plasma density and find that spatially localized ULF wave power enhancements are confined within high density patches in the afternoon sector (likely plasmaspheric plumes). The results have critical implications for empirical models of ULF wave power and radial diffusion coefficients. We highlight the necessity of improved characterization of the highly distorted storm-time cold plasma density distribution, in order to more accurately predict ULF wave power.

Plain Language Summary In the near-Earth space environment, the Earth's magnetic field oscillates at a variety of frequencies. Collections of charged particles, called plasma, in this region can interact with these magnetic waves with ultra low frequencies (ULF), transferring magnetic energy to the plasma. Sometimes these variations in the magnetic field are especially strong and wave power is increased. These periods are called geomagnetic storms. We used satellite measurements of ULF wave power to investigate how the power changes during geomagnetic storms, depending upon the size of the region and plasma environment. We show that the outer boundary of the Earth's magnetic field is key to describing how ULF wave power varies at different distances from Earth. We also show that the plasma conditions in the region are also important; during geomagnetic storms high density regions of plasma "trap" the ULF waves. These results improve our understanding how magnetic oscillations propagate through Earth's magnetic field, and show how regions of high wave power appear.

1. Introduction

The terrestrial magnetosphere is host to a wealth of electromagnetic fluctuations that communicate information and transfer energy across the magnetospheric system. Amongst the most interesting are those fluctuations occurring within the ultra low frequency (ULF) wave band with frequencies ranging from ~1–10 mHz (Jacobs et al., 1964). ULF waves play a crucial role in wider magnetospheric dynamics, associated with radial transport of the hazardous radiation belt population and resonant interactions with non-equilibrium particle distributions (e.g., Elkington et al., 2003).

Sources of ULF waves lie both internally and externally to the magnetosphere. External sources include Kelvin-Helmholtz instabilities at the magnetopause flanks (Chen & Hasegawa, 1974a, 1974b; Mann et al., 1999;

Rae et al., 2005; Southwood, 1974) and solar wind pressure fluctuations that buffet the dayside magnetopause (Kepko et al., 2002). Consequently, magnetospheric ULF wave power exhibits strong dependences and correlations with solar wind pressure, the southward component of the interplanetary magnetic field (IMF), as well as solar wind coupling functions that combine multiple solar wind parameters (Bentley et al., 2018; Koskinen & Tanskanen, 2002; Posch et al., 2003; Takahashi et al., 2012). Solar wind structures, such as coronal mass ejections and corotating interaction regions are associated with strong enhancements in ULF wave power (Hudson et al., 2014; Simms et al., 2010; Zong et al., 2009). Externally driven ULF waves have a broadband nature and an occurrence peaking across the dayside sector (Liu et al., 2009; Nosé et al., 1995; Nykyri, 2013; Pahud et al., 2009; Takahashi et al., 2016; Sandhu, Rae, Wygant, et al., 2021). Internal sources are associated with enhanced substorm activity and coupling to injected particle distributions (Baddeley et al., 2005; Engebretson & Cahill, 1981; Hughes, 1983; James et al., 2016; Nosé et al., 1998; Woch et al., 1990). In contrast to externally driven ULF waves, these narrowband ULF waves are most probable in the afternoon, dusk, and nightside magnetic local time (MLT) sectors. Although these internal sources are enhanced during geomagnetically active times (e.g., Sandhu, Rae, Wygant, et al., 2021), it has been demonstrated that external drivers are the dominant source of ULF wave power variability across the dayside inner magnetosphere (Bentley et al., 2019).

The propagation and behavior of these externally driven waves is very well-detailed in wave theory (e.g., Elsden & Wright, 2019). Southwood (1974) showed that compressional waves can propagate from the dayside magnetopause toward the Earth before reaching a turning point, beyond which the waves decay exponentially. In addition, these ULF waves can couple to transverse modes and drive resonant field line oscillations should they encounter field lines where the ULF wave frequency is equal to the field line eigenfrequency (Chen & Hasegawa, 1974a; Southwood, 1974), acting as another sink of the broadband compressional ULF wave power. Finally, sharp spatial gradients in plasma density are associated with similarly sharp changes in eigenfrequency (due to the dependence of the eigenfrequency on the Alfvén speed along a field line). Such a gradient exists across a well-defined plasmapause. It has been posited that the sharp change in eigenfrequencies can effectively reflect a large degree of Earthward propagating ULF wave power, resulting in a "barrier" that prevents the waves from accessing the plasmasphere (e.g., Lee et al., 2002). The region extending from the magnetopause to the plasmapause acts as a cavity for ULF waves, where a compressional mode wave can form a radially standing structure across the cavity (Kivelson & Southwood, 1986). This cavity can support various fast mode harmonics and will respond resonantly when driven over the appropriate frequency range (Allan et al., 1986).

In this study we consider how the characteristics of ULF wave power respond to geomagnetic storms, where dramatic enhancements in ULF wave power are observed across a wide radial extent of the inner magnetosphere (Sandhu, Rae, Wygant, et al., 2021). Large increases in observed ULF wave power are attributed predominantly to the elevated solar wind conditions (increased solar wind pressure and prolonged periods of strong southward IMF), and hence an enhanced external ULF wave source. However, as highlighted by Murphy et al. (2015), these active periods are also simultaneously associated with compressed magnetopause locations. Murphy et al. (2015) demonstrated that this earthward translation of the ULF wave source, as well as the magnitude of the source, plays an important role in contributing to the observed increase in wave power at a given ground magnetometer location.

Furthermore, the enhanced solar wind - magnetosphere coupling during geomagnetic storms drives increased convection electric fields and dynamics that significantly intensify internal magnetospheric conditions. The spatial distribution of plasma mass density in the inner magnetosphere undergoes drastic reconfiguration, including the depletion of plasma and plasmaspheric erosion (Kale et al., 2009; Katus et al., 2015; Sandhu et al., 2017), as well as a surge in heavy ion concentration (Kistler & Mouikis, 2016; Sandhu et al., 2017; Yue et al., 2019). In addition, the enhanced ring current acts to weaken and inflate the background magnetic field in the inner magnetosphere (Ganushkina et al., 2010; Jorgensen et al., 2004; Sandhu, Rae, & Walach, 2021). Overall, these storm time changes in the magnetic field and plasma result in a strong reduction in eigenfrequencies across the low density convection-dominated region outside the plasmasphere (the plasmatrough) (Kim et al., 2018; Sandhu et al., 2018; Rae et al., 2019; Wharton et al., 2020) and a sharp, well-defined boundary at the eroded plasmapause (Kale et al., 2007). As discussed by Wharton et al. (2020), the depressed eigenfrequencies and erosion of the plasmapause to low radial distances during

the storm main phase imply that ULF waves of a given frequency will couple at lower radial distances. These internal changes would significantly contribute to increased wave power at a given location during storm times. For example, Hartinger et al. (2010) provides observational evidence for the role of the plasmapause as a "barrier" to wave power, controlling the radial extent of ULF wave power propagation.

Therefore, it is reasonable to infer that the radial variation and dynamic evolution of ULF wave power depends on multiple factors: the magnitude of the external solar wind source, the location of the magnetopause, and the location of the plasmapause. In this case, perhaps a parameterization by radial distance would not adequately account for these dependences. With such complexity it is difficult to distinguish whether ULF wave power enhancements are due to enhanced wave sources or large scale magnetospheric structuring. Despite this we note that the overwhelming majority of previous statistical surveys of ULF wave power opt for this approach by parameterizing by L value (radial distance in the magnetic equatorial plane in Earth Radii) (e.g., Ali et al., 2016; Brautigam et al., 2005; Liu et al., 2009; Ozeke et al., 2014; Takahashi et al., 1992; Takahashi et al., 2016). In this study, we aim to determine the importance of both the magnetopause and plasmapause for understanding and predicting where compressional ULF wave power enhancements are observed during geomagnetic storms.

2. Data and Methodology

We conduct a statistical survey of compressional ULF wave power in the inner magnetosphere during geomagnetic storms using measurements provided by the Van Allen Probes (Mauk et al., 2013). The Van Allen Probes are two identically instrumented spacecraft that sampled the inner magnetosphere from October 2012 to July 2019 for Probe A, and from October 2012 to October 2019 for Probe B. The spacecraft operated in a 9 h orbit with an inclination of 10°. The orbital apogee was 5.8 Earth Radii (R_E), which precessed to cover all local times in less than 2 years. The orbital perigee was initially ~600 km, and underwent a series of lowering maneuvers from January 2019.

We use magnetic field observations provided by the Electric and Magnetic Field Instrument Suite and Integrated Science (EMFISIS) instrument (Kletzing et al., 2013). The full data set combines observations from both Probe A and Probe B, covering the period from January 2013 to October 2019.

The Van Allen Probes provide an optimal data set, due to the regular and repeated sampling of the inner magnetosphere for numerous geomagnetic storms. Furthermore, the choice of in situ sampling rather than ground magnetometer measurements of ULF waves allows us to minimize mapping uncertainties. During storm times, the magnetic field configuration is significantly distorted and mapping from the ionosphere to the equatorial magnetosphere can lead to non-negligible errors (e.g., Thompson et al., 2019).

2.1. Estimating ULF Wave Power

We estimate ULF wave power from the magnetic field measurements using an identical approach to Sandhu, Rae, Wygant, et al. (2021) and summarize the method here. First, a geomagnetic storm time period is identified and the magnetic field measurements are taken for the full event with a time resolution of 4 s. The background magnetic field is identified as the running average over a 20 min sliding window, and then subtracted from the magnetic field measurements to provide residual field observations. The residual field is transformed to a magnetic field-aligned coordinate system, which is defined by a parallel component aligned with the background magnetic field unit vector, an azimuthal component directed eastwards and perpendicular to the geocentric position vector, and a poloidal component that completes the Cartesian system. The parallel component of the residual magnetic field is subjected to a Morlet wavelet transform (Torrence & Compo, 1998), providing power spectral density estimates for the compressional magnetic field fluctuations.

The power spectral density, $P(f)$ [$nT^2\ Hz^{-1}$], is limited to a frequency range of 1 −15 mHz to focus on the ULF wave band. The power is then summed over this frequency range to estimate the total compressional ULF wave power, P [$nT^2\ Hz^{-1}$]. Samples with L values less than three were discarded from the data set as the field perturbations cannot be reliably separated from the rapidly varying background field at perigee. Samples with L values greater than six were excluded, as the Probes are located at significantly higher magnetic

latitudes where wave observations may not be comparable to observations at $L < 6$ when the Probes are at quasi-equatorial latitudes. The L value is defined as the radial location in the magnetic equatorial plane. The data set is also restricted to cover samples located in the morning and noon MLT sectors ($06 < \text{MLT} \leq 15$ h). This MLT sector will focus on ULF waves originating from external solar wind sources, and minimize the presence of ULF waves originating from internal sources that are prevalent across the dusk and nightside sectors. The analysis is applied to both Probe A and Probe B observations for all storms covered by the Van Allen Probes data set, providing a large data set of compressional ULF wave power, P [nT^2 Hz^{-1}].

2.2. Identifying Geomagnetic Storms

This study focuses exclusively on geomagnetic storm times. To determine storm periods, we employ the automated algorithm of Walach and Grocott (2019), which identifies storms from time series of the Sym-H index (Iyemori, 1990). Furthermore, the algorithm provides timings for the start and end of each storm phase (initial, main, and recovery phase).

The Walach and Grocott (2019) algorithm operates by first identifying storm occurrences as any instance where the Sym-H index crosses below a threshold of −80 nT. For each storm, the start of the recovery phase is defined as the time of the Sym-H index minimum. The start of the main phase and the end of the recovery phase are defined using a quiet time threshold of −15 nT, marking the times immediately prior to and after the Sym-H index minima where the Sym-H index is less than the quiet time threshold. The initial phase contains a maximum in the Sym-H index. The start of the initial phase is defined as the time immediately prior to the Sym-H index maximum where the Sym-H index is at the quiet time threshold. The storm time threshold (−80 nT) and the quiet time threshold (−15 nT) follow definitions by Hutchinson et al. (2011).

The algorithm provides 45 storms for analysis during the Van Allen Probes data set. As expected, wave power samples corresponding to the main and recovery phases are associated with enhanced solar wind conditions compared to the initial phase. Further details on the solar wind (speed and southward IMF component) and Sym-H values associated with each phase is included in Figure S1 of the supporting information.

2.3. Identifying Magnetopause and Plasmapause Locations

In order to explore the dependence of ULF wave power on the location of the magnetopause and plasmapause boundaries, we require concurrent estimates of the boundary locations for every sample of wave power, P.

Magnetopause locations are estimated using the Shue et al. (1998) model of the magnetopause, which is an empirically derived model parameterized by the solar wind dynamic pressure and the IMF B_Z component. Solar wind parameters are provided by the NASA/GSFC's OMNI data set at a time resolution of 1 min through OMNIWeb (https://omniweb.gsfc.nasa.gov/index.html). The radial distance of the magnetopause in R_E, L_{MP}, is taken for each sample of P for the MLT location of the spacecraft. The use of the Shue et al. (1998) model allowed minimal reductions in the data set, as opposed to relying on conjunctions with magnetopause crossings. The validity of the Shue et al. (1998) magnetopause model during geomagnetic storms was verified through an independent comparison to magnetopause crossings identified by Staples et al. (2020). The data base of magnetopause crossings from Staples et al. (2020) includes identifications from Plaschke et al. (2009), Raymer (2018), and Case and Wild (2013). Figure S2 in the supporting information demonstrates that, on average, the measured magnetopause locations across the dayside magnetosphere are well represented by the Shue et al. (1998) model for all storm phases.

Figures 1a–1c shows the probability density functions of the magnetopause location, L_{MP}, for all samples in the data set (dark blue line distributions), where each panel shows data binned for a given storm phase. We observe that the location of the magnetopause is variable, spanning a range of 10 R_E during storms. During the initial phase, the most probable magnetopause location is between 10–11 R_E. This experiences an earthward displacement to 8–10 R_E during the main phase, and then returns to 10–11 R_{E} during the recovery phase. The earthward displacement during the main phase is driven by enhanced solar wind pressure and a strongly southward IMF.

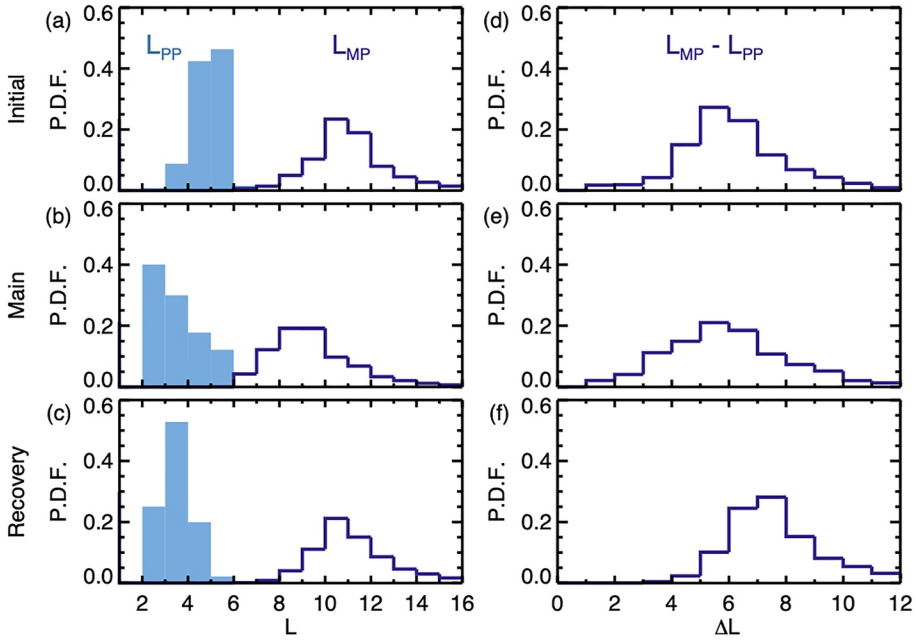

Figure 1. Probability density functions of (a–c) L values of the magnetopause (dark blue line) and the plasmapause (light blue solid) locations, and (d–e) the difference in L value, ΔL, between the magnetopause and plasmapause. Distributions are shown for the storm (a and d) initial phase (b and e) main phase, and (c and f) recovery phase.

Plasmapause locations are obtained from measurements of the total electron density, n_e [cm^{-3}], provided by the EMFISIS instrument on-board the Van Allen Probes spacecraft (Kurth et al., 2015). A plasmapause crossing is defined as the location where n_e crosses a threshold value of 100 cm^{-3}, taking each half-orbit independently. If density observations are unavailable then the upper hybrid-frequency, f_{UH} [Hz], is used, identifying the location where f_{UH} drops below $\sqrt{f_{CE} + (100 \times 8980^2)}$ where f_{CE} is the electron cyclotron frequency [Hz]. If the threshold is crossed multiple times during a half-orbit, the plasmapause location is taken as the innermost crossing. The innermost crossing was chosen to avoid misidentifying any density irregularities (e.g., plumes) in the plasmatrough as the plasmapause. We highlight that all plasmapause crossings are manually verified through visual inspection of the n_e and f_{UH} observations. The temporally closest plasmapause crossing is taken for each sample of P, provided that the crossing occurred within 9 h (1 orbital period for the Van Allen Probes). The data set of plasmapause crossings has been established for a time period of 2012–2016, restricting the subsequent analysis to this time period.

Figures 1a–1c show the probability density functions of the plasmapause L value, L_{PP}, across the full data set (blue solid distributions), where each panel shows data binned for a given storm phase. Similar to the magnetopause locations, the plasmapause occupies a range of locations in each storm phase, with the distributions extending over multiple L values. During the initial phase, the plasmapause is observed most frequently between $4 < L_{PP} \leq 6$. During the main phase the distribution is shifted to significantly lower L values, with the peak located between $2 < L_{PP} \leq 3$, and exhibits a negatively skewed distribution shape. During the recovery phase, the distribution asymmetry is reduced and the peak is located between $3 < L_{PP} \leq 4$. The erosion and Earthward displacement of the plasmapause is driven by enhanced convective electric fields in the inner magnetosphere, resulting from more geoeffective solar wind conditions. It is noted that the identification technique includes plasmapause boundaries with different radial gradients, where we do not differentiate between sharp, well-defined boundaries or broader boundaries. Previous studies suggest that the plasmapause has an increased radial density gradient during the main phase of geomagnetic storms (e.g., Kale et al., 2007), although the impact of detailed plasmapause properties on ULF wave dynamics is relegated to a later study.

Figures 1a–1c provides useful insight into the locations of the boundaries during each storm phase but it is also important to consider the difference in the locations, as this defines the cavity size for ULF wave

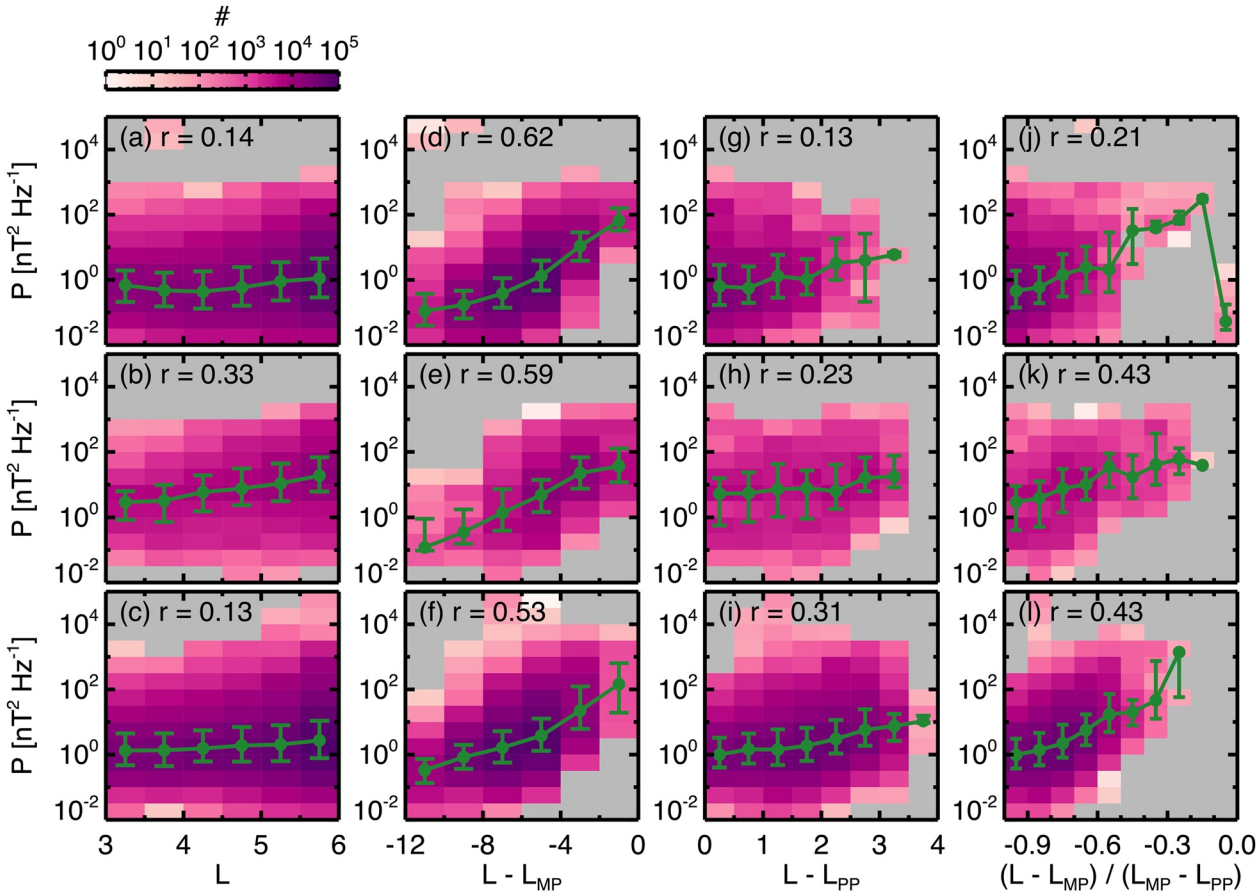

Figure 2. Samples are binned for a chosen radial parameter and power, P [nT^2 Hz^{-1}], where the occurrence is indicated by the color of the bin. The median and interquartile range as a function of the radial parameter is represented by the green profile and bars. The radial parameters considered are (a–c) L value (d–f) $L - L_{MP}$ (g–i) $L - L_{PP}$, and (j–l) $L - L_{MP}/L_{MP} - L_{PP}$. Data is also binned for the (a, d, g, and j) initial phase (b, e, h, and k) main phase, and (c, f, i, and l) initial phase, as labeled.

propagation. Figures 1d–1f shows the distribution of the difference between the magnetopause and plasmapause locations, $\Delta L = L_{MP} - L_{PP}$. Although the distribution widths indicate variability in the size of the cavity throughout all phases, we observe that the average cavity size remains relatively constant during initial and main phases with a typical size of $5 < \Delta L \leq 6$, and is slightly expanded during the recovery phase with the distribution peaking at $7 < \Delta L \leq 8$. Interestingly, the relatively constant cavity size during geomagnetic storms contradicts results from ionospheric observations. Walach and Grocott (2019) uses SuperDARN Super Dual Auroral Radar Network (SuperDARN) observations to infer an increase in the cavity size during the main phase of the storm. The apparent discrepancy is attributed to non-negligible changes in the mapping of field lines from the ionosphere to the magnetosphere within the highly distorted storm time magnetosphere.

3. Results

The data set of compressional ULF wave power, P, is statistically analyzed to assess storm time variations and dependences on the magnetopause and plasmapause boundaries. Figures 2a–2c show the distribution of P binned for L value. The color of each bin represents the number of samples in L - P space; the green profile and bars show the median and interquartile range of P as a function of L value. Each panel corresponds to a given storm phase. Figures 2a–2c show enhancements in P during the storm main phase. Although these enhancements occur across all L values monitored here, the magnitude of the increase is clearly larger at higher L values, where an increase by more than order of magnitude is observed for $5 < L \leq 6$. Consequently, although the radial dependence of P is relatively weak during the initial phase, the average profile

is markedly steeper during the main phase. Figures 2a–2c also reveals the high variability in P, where the occurrence distributions span a large range of values across all L.

Figure 2 also considers how combining the magnetopause and plasmapause boundary locations with the L value may improve parameterization of the compressional ULF wave power. For samples within each panel, a Spearman's correlation test is applied to assess the relationship between P and the relevant radial parameter, and the resulting correlation coefficient, r, is labeled in Figure 2. The Spearman's correlation test is a nonparametric statistical test that determines the strength and direction of the monotonic relationship between two variables (Spearman, 1987). Radial parameters that are associated with a higher correlation can be inferred to (directly or indirectly) relate to an important physical property of ULF wave propagation. Figure 2 considers the following radial parameters:

1. The L value (Figures 2a–2c), where the L value closely relates to the background magnetic field.
2. The L value relative to the magnetopause, $L - L_{MP}$ (Figures 2d–2f). This radial parameter represents the location relative to the external ULF wave power source where the power is expected to maximize.
3. The L value relative to the plasmapause, $L - L_{PP}$ (Figures 2g–2i), which represents the location relative to the ULF wave power "barrier" where the power is expected to minimize.
4. The cavity normalised location relative to the magnetopause $(L - L_{MP})/(L_{MP} - L_{PP})$ (Figures 2j–2l). This parameter orders by both the expected maximum (at the magnetopause) and minimum (at the plasmapause) in ULF wave power.

We note that although Figure 2 includes data across the wide MLT range of $06 < \text{MLT} < 15$, the trends are qualitatively representative of smaller MLT subsets across the sector, although the magnitude of the correlation coefficients vary.

Overall, the correlation coefficients peak when ordered by $L - L_{MP}$ (Figures 2d–2f), with r values ranging from 0.53 to 0.62. The resulting median profiles exhibit a clear radial dependence, where values peak close to the magnetopause (toward $L - L_{MP} = 0$) with a steady decrease toward the Earth. Comparing the median profiles, the difference between storm phases is less pronounced than for the L parameterization. The close similarity between median profiles suggests that a significant degree of variability is accounted for by the magnetopause location. However, we also note that the occurrences (indicated by bin color) demonstrate that increased wave power is still observed for a given $L - L_{MP}$ during the main and recovery phases compared to the initial phase. We attribute this enhanced wave power to elevated solar wind conditions, such as increased solar wind speed and large solar wind dynamic pressure fluctuations during the main phase of geomagnetic storms, that are effective at generating ULF wave power within the magnetosphere (e.g., Kilpua et al., 2015).

The analysis also considers the location of the plasmapause, included both independently (Figures 2g–2i) as well as in conjunction with the magnetopause (Figures 2j–2l). However, the lower correlation coefficients and flatter profiles suggest that the plasmapause location is not a particularly significant variable that shapes the radial distribution of observed P values, as compared to L_{MP}. Although we note that, in general, the parameterisations still outperform correlations with the L value alone.

The statistical analysis shown in Figure 2 includes data spanning a range of solar wind conditions (see Figures S1b and S1c). Although details are omitted for brevity, we note that the qualitative trends remain consistent for different levels of solar wind speed and no significant evidence for biases of the correlation coefficients with solar wind speed are observed. Future work and empirical modeling will explore and quantify dependences on solar wind conditions in further detail.

3.1. Dependence on Cold Plasma Density Distributions

The results shown in Figure 2 suggest that the plasmapause may not be an important "barrier" to compressional ULF wave power. However, these results represent an average over the full data set, so we also consult individual events for further analysis. In Figure 3 we present a representative case study during August 2014, where the Van Allen Probes sampled the dayside magnetosphere during a geomagnetic storm. Figures 3a–3c shows time series of the the Sym-H index, solar wind speed, and IMF B_Z component, to provide contextual information on the storm characteristics and solar wind conditions. We observe that the solar

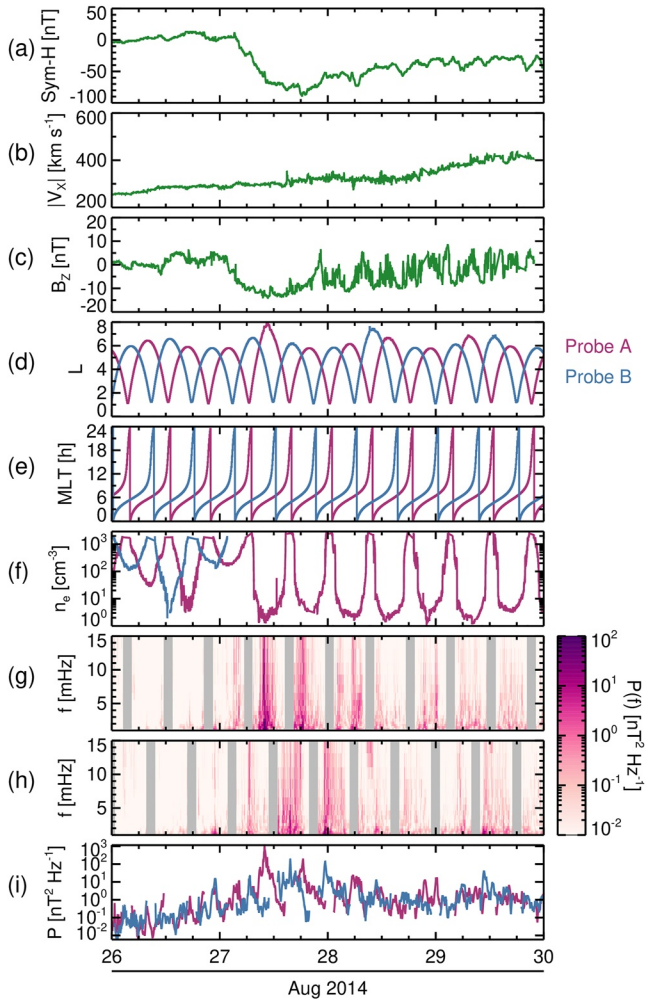

Figure 3. Time series for August 26–30, 2014, showing the (a) Sym-H index [nT], (b) Earthward component of the solar wind speed, $|V_X|$ [km s^{-1}], and (c) southward interplanetary magnetic field component, B_Z [nT]. Panels (d–i) show time series for the Van Allen Probes A (pink) and B (blue). We show the (d) L value and (e) magnetic local time [h] of the spacecraft location, and (f) total electron density, n_e [cm^{-3}]. Panels (g and h) show power, $P(f)$ [nT^2 Hz^{-1}], as a function of frequency, f [mHz], and time for Probe A and Probe B, respectively. Panel (i) shows the power, P [nT^2 Hz^{-1}], summed over the ultra low frequencies wave band.

wind speed progressively and steadily increased throughout the event. During the storm main phase (period of sharp decline in the Sym-H index during August 27, 2014), the IMF had a strong southward component with B_Z values reaching below −10 nT. Figures 3d and 3e shows the L value and MLT of Probe A (pink) and Probe B (blue), indicating the orbital apogee was located at approximately 06 MLT. Figure 3f shows the total electron density, n_e [cm^{-3}], observed by the EMFISIS instrument. Note that a data gap in n_e measurements occurred for Probe B for the majority of this interval. Throughout the event the Probes sample both the plasmaspheric population (n_e greater than ∼100 cm^{-3}) and the plasmatrough (the low density region outside the plasmasphere with densities as low as ∼1 cm^{-3}). Figures 3g and 3h show power-frequency spectra for Probe A and Probe B, respectively, where the power is indicated by color. Figure 3i shows the summed wave power across the ULF wave band as a function of time. Large broadband enhancements in wave power are evident during the storm main phase, peaking for Probe A at approximately 10:00 UT on August 27, 2014, and then decaying to pre-storm values in the recovery phase. The broadband nature and coincidence with the strong southward IMF suggests an enhancement in the external source of ULF waves. However, it is difficult to ascertain the radial structure of the ULF wave enhancement from the time series shown.

We consider the inbound pass of Probe A occurring from 10:25 UT August 27, 2014 to 2015:25 UT August 27, 2014, which corresponds to the period of enhanced wave power. The time series shown in Figure 3 are binned for L value using an L bin width of 0.2 over the time interval of interest, and median values are plotted as a function of L value in Figure 4. Figures 4a–4c shows the median Sym-H index, solar wind speed, and IMF B_Z component. The values are relatively constant during the period, evidencing that stable external and internal conditions were maintained throughout the pass. Hence, variations in density and wave power are likely to be spatial features. Figure 4d shows the probability density function of the subsolar magnetopause locations, L_{MP0}, during the pass. The subsolar location is chosen to remove variations due to the spacecraft MLT, and identify any dislocations of the magnetopause boundary. The distribution of L_{MP0} is narrow and peaked at ∼8, suggesting a compressed but quasi-stationary magnetopause. Figure 4e shows the MLT location of the spacecraft, indicating a traversal through the morning MLT sector. It is assumed that the MLT variations within the sampled sector are minor compared to the L dependence for this pass. The median electron density, n_e [cm^{-3}], is shown in Figure 4f. At $L < 3$ the spacecraft observes high density plasma, typical of the plasmasphere, with a sharp drop at the plasmapause with densities decreasing by more than one order of magnitude at $L \sim 3$. For $L > 3$, the density exhibits a general power law decrease with L value and is characteristic of the plasmatrough region. Figures 4g and 4h show the median power-frequency spectra and summed ULF wave power, respectively. We observe a monotonic decrease in wave power with decreasing L value (across all frequencies). The power is largest close to the magnetopause, and moving Earthwards, we observe that the power has decayed to a very low value ($P < 1$ nT^2 Hz^{-1}) before the plasmapause boundary is encountered.

Although the event examined in Figures 3 and 4 is representative of events where the Van Allen Probes had a pre-noon apogee, event analysis revealed unique dynamics in the post-noon sector. A corresponding representative example for the post-noon sector is shown in Figure 5, where time series are displayed in the same format as Figure 3. Figure 5 focuses on a orbital pass from 23:00 UT August 26, 2015 to 09:00 UT August 27, 2015, where this interval is during the main phase of a geomagnetic storm. During this orbit,

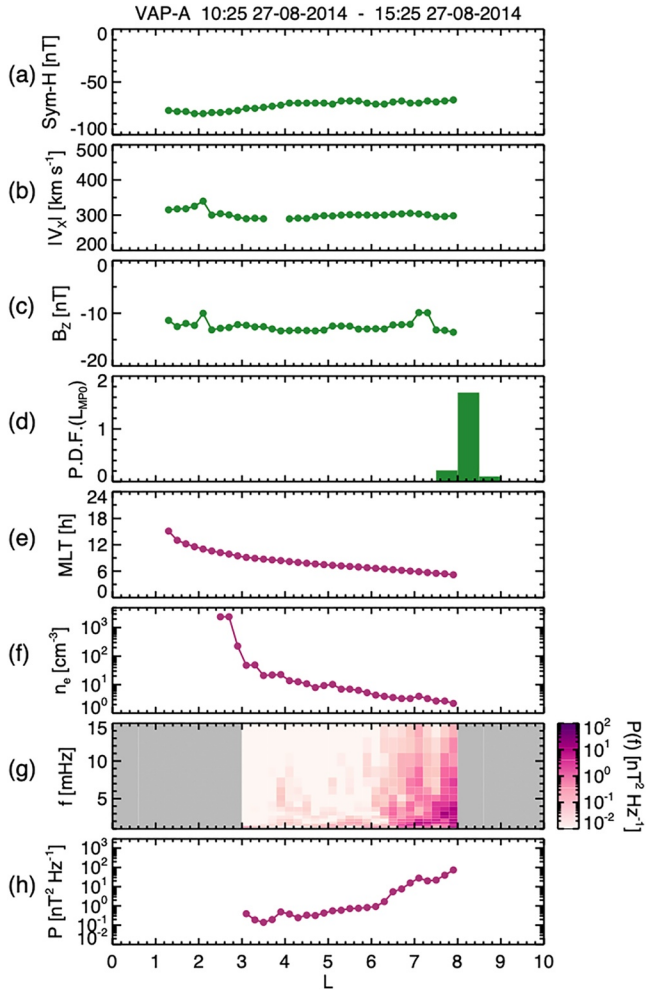

Figure 4. Van Allen Probe A data from 10:25 UT August 27, 2014 to 2015:25 UT August 27, 2014 are binned for L value, using an L bin width of 0.2. For samples in each bin, the median values of the (a) Sym-H index [nT], (b) Earthward component of the solar wind speed, $|V_X|$ [km s^{-1}], and (c) Southward interplanetary magnetic field component, B_Z [nT] are shown. Panel (d) shows the probability density distribution of the subsolar magnetopause location during the considered time period. The median values of the (e) magnetic local time [h] location of the spacecraft, (f) total electron density, n_e [cm^{-3}], (g) power, $P(f)$ [nT^2 Hz^{-1}], as a function of frequency, f [mHz], and (h) power, P [nT^2 Hz^{-1}], summed over the Ultra Low Frequencies wave band are also shown.

the Sym-H index (Figure 5a) varied around ∼−80 nT, the solar wind speed (Figure 5b) was steady at ∼360 km s^{-1} throughout the period, and the IMF B_Z (Figure 5c) was initially strongly southward at ∼−10 nT followed by a sharp jump to ∼0 nT at approximately 04:30 UT. During the outbound pass, we can confidently assume that the external solar wind conditions were stable. For this event the Van Allen Probes sampled the dayside MLT sector with an apogee at ∼15 MLT. The electron density time series (noting a data gap in n_e observations for Probe A) shows that during the outbound pass, Probe B entered a low density ($n_e < 100$ cm^{-3}), plasmatrough-like region at approximately 00:30 UT. It traversed the plasmatrough until ∼02:15 UT, when a localized enhancement in n_e was encountered until around 04:00 UT when n_e returned to the low density environment. Another, more localized, enhancement was observed briefly at ∼05:00 UT. Probe B then crossed a well-defined plasmapause and entered the plasmasphere at approximately 06:50 UT. Consulting the ULF wave power observations (Figures 5g–5i) unveils some interesting features. During the intervals where Probe B observed localized, high density plasma embedded within the plasmatrough, we also observe highly elevated, synchronous, and broadband ULF wave power with $P > 10^2$ nT^2 Hz^{-1}. Elsewhere at lower L values and in the plasmatrough, the power is significantly lower ($P \sim 10^0$ nT^2 Hz^{-1} for Probe B). Note that we take more confidence in observations during the outbound passes, where the IMF B_Z is stable, compared to the inbound pass where variability in the solar wind parameters and Sym-H index were observed.

The events examined in Figures 3–5 suggest a density-dependent relationship between the main phase power enhancements and radial location. Figure 6 explores this dependence further for compressional ULF wave power observations during the main phase of a storm. Each panel shows the samples binned for L value and n_e, where the color of the bin represents the number of samples (Figures 6a–6c) and the median value of P (Figures 6d–6f). The samples are also binned by MLT sector, as labeled, to allow local time dependences to be examined. Note that the data has been ordered by L value. Although parameterization by $L - L_{MP}$ improves correlation (Figure 2), the L value allows us to directly relate the location to the expected cold plasma density spatial distributions. Figures 6a–6c shows that at $L < 4$, the density distributions are similar with MLT. High density plasma ($n_e > 100$ cm^{-2}) typical of the plasmasphere is frequently sampled and Figure 1b shows that at these locations the probability of being within the plasmasphere is more than 50%. However, at higher L values ($L > 5$) we observe MLT-dependent distributions of sample occurrence with n_e. Figure 6a shows that for 06 = MLT < 09, the typical n_e values are low with the peak occurrence located below 10 cm^{-3}. In contrast, Figures 6b and 6c shows that the distributions are wider in the noon and post-noon sectors and high density plasma is frequently sampled.

Figures 6d–6f shows the corresponding median ULF wave power. As expected, higher P values are observed at higher L values (see also Figure 2b). However, we note that high P values are not strictly limited to low density, plasmatrough-like plasma. Particularly in the noon and post-noon sectors (Figures 6e and 6f), we observe high median wave power ($P > 10$ nT^2 Hz^{-1}) frequently in regions where the density exceeds 100 cm^{-3}, especially for higher L values that are likely to be located outside of the plasmapause. This corroborates the event study results shown in Figure 5, where localized, high-density regions of plasma located outside of the plasmapause can be associated with high ULF wave power. These high density regions

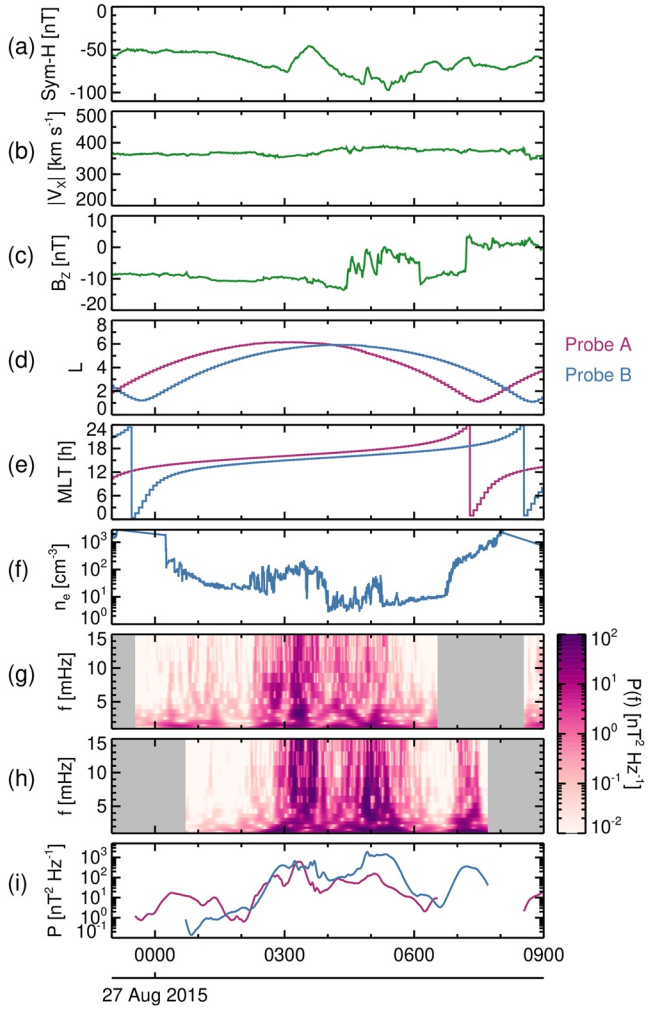

Figure 5. Time series for 23:00 UT August 26, 2015 to 09:00 UT August 27, 2015, following the same format as Figure 3.

are likely plasmaspheric plumes, given their location in MLT being coincident with where plumes are most frequently observed (Darrouzet et al., 2008; Usanova et al., 2013).

4. Interpretation and Concluding Remarks

The statistical and event study analysis confirms some expected and previously observed features of externally driven compressional ULF wave propagation in the inner magnetosphere during geomagnetic storms, and also demonstrates the importance of phenomena that has received comparatively less attention. In direct agreement with previous results (e.g., Sandhu, Rae, Wygant, et al., 2021; Simms et al., 2010), we report significant enhancements in ULF wave power during the main phase of geomagnetic storms, associated with elevated solar wind conditions and a high level of solar wind - magnetosphere coupling. The main phase enhancements occur across all observed L values, with larger enhancements at higher L values.

Through a consideration of the magnetopause and plasmapause boundaries, we determine that a significant part of the ULF wave power enhancement can be accounted for by the compressed magnetopause during the storm main phase. As well as an increase in the magnitude of the external ULF wave source, this source is located closer to the inner magnetosphere, confirming previous results from Murphy et al. (2015). Although the magnetopause is observed to play an important role in determining the radial distribution of wave power, we demonstrate that the plasmapause itself is perhaps less important. Figures 2d–2f and Figures 2j–2l show that the broadband wave power decays rapidly away from the magnetopause, reaching pre-storm values before the plasmapause is encountered. Furthermore, the inclusion of the plasmapause position in describing the radial location does not improve the correlation of wave power (Figure 2) and we observe no clear evidence for a sharp reduction in wave power across the plasmapause (Figure 4). The result somewhat contradicts work suggesting that the sharp density gradient at the plasmapause generates an effective "barrier" such that high ULF wave power exists immediately outside the boundary and much lower wave power occupies the plasmaspheric region (e.g., Lee et al., 2002, and others).

So why do previous studies, such as the statistical analysis of Hartinger et al. (2010), suggest that the plasmapause plays an important role? Hartinger et al. (2010) presented a statistical survey of Pc5 waves during periods where $K_P \leq 3$, and reported that at a given L value samples within the plasmasphere have lower ULF wave power than samples outside the plasmapause. It is key to note that the Hartinger et al. (2010) analysis is not representative of geomagnetically active times, and so the results should not be directly compared to the storm time analysis conducted here. Perhaps the difference in results suggest that the plasmapause is a more effective "barrier" during quiet geomagnetic conditions or smaller storms where it is located closer to the magnetopause. During storm times the extreme Earthward location may mean that the eroded plasmapause is less important in reducing broadband wave power. Instead, we present results suggesting that the eigenfrequency profile in the plasmatrough is more effective and dominant in shaping the "penetration" of compressional ULF waves, than compared to the sharp plasmaspheric boundary. Studies such as Sandhu et al. (2018), Rae et al. (2019) and Wharton et al. (2020) demonstrate strong storm time variations in the radial eigenfrequency profile that have a frequency-dependent impact on how ULF wave propagate within the plasmatrough region. Future analysis will explore how the frequency distribution of storm time externally driven compressional waves relate to these average storm time eigenfrequency profiles.

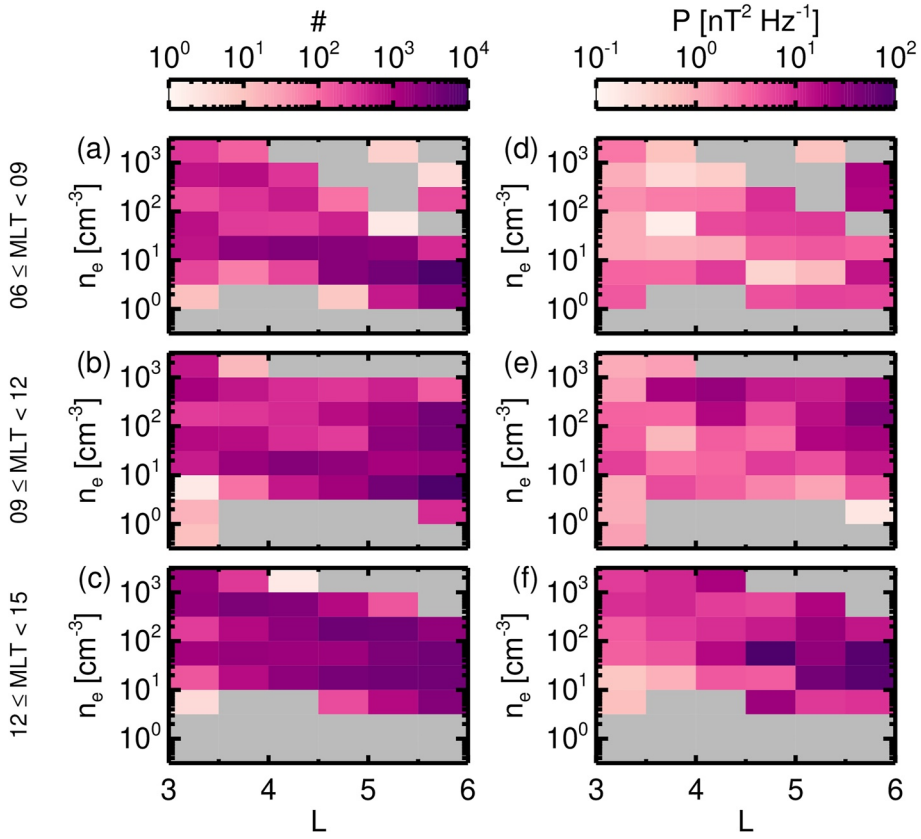

Figure 6. Data during the storm main phase are binned for L value and total electron density, n_e [cm^{-3}]. Panels (a–c) show the number of samples in each bin, and panels (d–f) show the median power, P [nT^2 Hz^{-1}], for samples within each bin. Data is also binned for magnetic local time (MLT), where panels (a and d) show data within 06 ≤ MLT < 09, panels (b and e) show data within 09 ≤ MLT < 12, and panels (c and f) show data within 12 ≤ MLT < 15, as labeled.

Although the plasmapause may not be significantly influential in the radial propagation of ULF compressional waves, we instead find that the cold plasma density distribution can be statistically important in a different way. As shown in Figures 5 and 6, high wave power can be confined within regions of high density plasma that is, located outside of the expected plasmasphere at high L values. These instances are likely during the storm main phase and in the noon and post-noon MLT sectors. During geomagnetically active periods, it is well-established that strong enhancements in solar wind - magnetosphere coupling and the convective electric field significantly distort and erode the plasmasphere, resulting in the formation of a plasmaspheric plume and detached plasmaspheric plasma within the afternoon sector plasmatrough (Chappell, 1972; Goldstein et al., 2019; Sandhu et al., 2017; Spasojević et al., 2003). We infer that it is these plumes and detached material that is, sampled at high L values. Previous studies have demonstrated that the spatially localized, high density plasma can generate a local cavity for compressional ULF waves, and that these regions can effectively "trap" wave power within them (Degeling et al., 2018). We suggest that the event shown in Figure 5 is a prime example of this phenomenon, and the results shown in Figure 6 suggest that the "trapping" of highly enhanced wave power in high density regions is statistically likely during geomagnetic storms.

Overall, these results have significant implications for our understanding of storm time ULF wave dynamics, particularly efforts to model the magnitude of ULF wave driven radial diffusion during active periods (e.g., Brautigam & Albert, 2000; Ozeke et al., 2014; Sandhu, Rae, Wygant, et al., 2021). We demonstrate that parameterization by the L value alone is comparatively inadequate in describing the radial variation of wave power during active periods. Instead, statistical parameterisations may benefit from also incorporating the magnetopause location (either directly or through the inclusion of solar wind characteristics (e.g., Bentley et al., 2018)) to reduce variability in observed values. However, it is clear that an area warranting significant

attention is the need for accurate descriptions of the cold plasma density distribution during geomagnetic storms. Specifically, the occurrence, location, and morphology of plasmaspheric plumes and detached high density material is crucial. We have demonstrated that these regions, although spatially localized, are responsible for significantly elevated ULF wave power, which may potentially play an important role in wider magnetospheric dynamics. We aim to explore the impact of these "patches" of enhanced ULF wave power on the radial diffusion of radiation belt electrons in future work.

Data Availability Statement

The Van Allen Probes data are publicly available online (https://cdaweb.gsfc.nasa.gov/index.html/). We acknowledge use of NASA/GSFC's Space Physics Data Facility's OMNIWeb service for the provision of the solar wind and Sym-H index data. The data sets used are publicly available online (https://omniweb.gsfc.nasa.gov/index.html).

Acknowledgments
J. K. Sandhu is supported by NERC grants NE/P017185/2 and NE/V002554/2. I. J. Rae is supported by NERC grants NE/P017185/2 and NE/V002554/2, and STFC Consolidate grant ST/V006320/1. F. A. Staples is supported by a Science and Technology Funding Council (STFC) studentship. D. P. Hartley is supported under JHU/APL contract 921647 under NASA Prime contract NAS5-01072. M.-T. Walach is supported by NERC grant NE/T000937/1. T. Elsden is supported by a Leverhulme Trust Early Career Fellowship (ECF-2019-155) and the University of Leicester. K. R. Murphy is partially funded by NASA ROSES Guest Investigator 18-HGIO18_2-0122 and Space Weather Operations to Research 18-HSWO2R18-0010. We thank the EMFISIS instrument team for data provision.

References

Ali, A. F., Malaspina, D. M., Elkington, S. R., Jaynes, A. N., Chan, A. A., Wygant, J., & Kletzing, C. A. (2016). Electric and magnetic radial diffusion coefficients using the Van Allen Probes data. *Journal of Geophysical Research: Space Physics*, *121*(10), 9586–9607. https://doi.org/10.1002/2016JA023002

Allan, W., White, S., & Poulter, E. (1986). Impulse-excited hydromagnetic cavity and field-line resonances in the magnetosphere. *Planetary and Space Science*, *34*(4), 371–385. https://doi.org/10.1016/0032-0633(86)90144-3

Baddeley, L. J., Yeoman, T. K., & Wright, D. M. (2005). HF doppler sounder measurements of the ionospheric signatures of small scale ULF waves. *Annales Geophysicae*, *23*(5), 1807–1820. https://doi.org/10.5194/angeo-23-1807-2005

Bentley, S. N., Watt, C. E. J., Owens, M. J., & Rae, I. J. (2018). ULF wave activity in the magnetosphere: Resolving solar wind interdependencies to identify driving mechanisms. *Journal of Geophysical Research: Space Physics*, *123*(4), 2745–2771. https://doi.org/10.1002/2017JA024740

Bentley, S. N., Watt, C. E. J., Rae, I. J., Owens, M. J., Murphy, K., Lockwood, M., & Sandhu, J. K. (2019). Capturing uncertainty in magnetospheric ultralow frequency wave models. *Space Weather*, *17*(4), 599–618. https://doi.org/10.1029/2018SW002102

Brautigam, D. H., & Albert, J. M. (2000). Radial diffusion analysis of outer radiation belt electrons during the October 9, 1990, magnetic storm. *Journal of Geophysical Research*, *105*(A1), 291–309. https://doi.org/10.1029/1999JA900344

Brautigam, D. H., Ginet, G. P., Albert, J. M., Wygant, J. R., Rowland, D. E., Ling, A., & Bass, J. (2005). CRRES electric field power spectra and radial diffusion coefficients. *Journal of Geophysical Research*, *110*(A2), A02214. https://doi.org/10.1029/2004JA010612

Case, N. A., & Wild, J. A. (2013). The location of the earth's magnetopause: A comparison of modeled position and in situ cluster data. *Journal of Geophysical Research: Space Physics*, *118*(10), 6127–6135. https://doi.org/10.1002/jgra.50572

Chappell, C. R. (1972). Recent satellite measurements of the morphology and dynamics of the plasmasphere. *Reviews of Geophysics*, *10*(4), 951–979. https://doi.org/10.1029/RG010i004p00951

Chen, L., & Hasegawa, A. (1974a). A theory of long-period magnetic pulsations: 1. Steady state excitation of field line resonance. *Journal of Geophysical Research*, *79*(7), 1024–1032. https://doi.org/10.1029/JA079i007p01024

Chen, L., & Hasegawa, A. (1974b). A theory of long-period magnetic pulsations: 2. Impulse excitation of surface eigenmode. *Journal of Geophysical Research*, *79*(7), 1033–1037. https://doi.org/10.1029/JA079i007p01033

Darrouzet, F., De Keyser, J., Décréau, P. M. E., El Lemdani-Mazouz, F., & Vallières, X. (2008). Statistical analysis of plasmaspheric plumes with cluster/whisper observations. *Annales Geophysicae*, *26*(8), 2403–2417. https://doi.org/10.5194/angeo-26-2403-2008

Degeling, A. W., Rae, I. J., Watt, C. E. J., Shi, Q. Q., Rankin, R., & Zong, Q.-G. (2018). Control of ULF wave accessibility to the inner magnetosphere by the convection of plasma density. *Journal of Geophysical Research: Space Physics*, *123*(2), 1086–1099. https://doi.org/10.1002/2017JA024874

Elkington, S. R., Hudson, M. K., & Chan, A. A. (2003). Resonant acceleration and diffusion of outer zone electrons in an asymmetric geomagnetic field. *Journal of Geophysical Research*, *108*(A3), 1116. https://doi.org/10.1029/2001JA009202

Elsden, T., & Wright, A. N. (2019). The effect of fast normal mode structure and magnetopause forcing on FLRS in a 3-D waveguide. *Journal of Geophysical Research: Space Physics*, *124*(1), 178–196. https://doi.org/10.1029/2018JA026222

Engebretson, M. J., & Cahill, L. J., Jr. (1981). Pc5 pulsations observed during the June 1972 geomagnetic storm. *Journal of Geophysical Research*, *86*(A7), 5619–5631. https://doi.org/10.1029/JA086iA07p05619

Ganushkina, N. Y., Liemohn, M. W., Kubyshkina, M. V., Ilie, R., & Singer, H. J. (2010). Distortions of the magnetic field by storm-time current systems in earth's magnetosphere. *Annales Geophysicae*, *28*(1), 123–140. https://doi.org/10.5194/angeo-28-123-2010

Goldstein, J., Pascuale, S., & Kurth, W. S. (2019). Epoch-based model for stormtime plasmapause location. *Journal of Geophysical Research: Space Physics*, *124*(6), 4462–4491. https://doi.org/10.1029/2018JA025996

Hartinger, M., Moldwin, M. B., Angelopoulos, V., Takahashi, K., Singer, H. J., Anderson, R. R., et al. (2010). Pc5 wave power in the quiet-time plasmasphere and trough: CRRES observations. *Geophysical Research Letters*, *37*(7), L07107. https://doi.org/10.1029/2010GL042475

Hudson, M. K., Baker, D. N., Goldstein, J., Kress, B. T., Paral, J., Toffoletto, F. R., & Wiltberger, M. (2014). Simulated magnetopause losses and Van Allen Probe flux dropouts. *Geophysical Research Letters*, *41*(4), 1113–1118. https://doi.org/10.1002/2014GL059222

Hughes, W. J. (1983). Hydromagnetic waves in the magnetosphere. In R. L. Carovillano, & J. M. Forbes (Eds.), *Solar-terrestrial physics* (pp. 453–477). Dordrecht. Springer Netherlands. https://doi.org/10.1007/978-94-009-7194-3_18

Hutchinson, J. A., Wright, D. M., & Milan, S. E. (2011). Geomagnetic storms over the last solar cycle: A superposed epoch analysis. *Journal of Geophysical Research*, *116*(A9), A09211. https://doi.org/10.1029/2011JA016463

Iyemori, T. (1990). Storm-time magnetospheric currents inferred from mid-latitude geomagnetic field variations. *Journal of Geomagnetism and Geoelectricity*, *42*, 1249–1265. https://doi.org/10.5636/jgg.42.1249

Jacobs, J. A., Kato, Y., Matsushita, S., & Troitskaya, V. A. (1964). Classification of geomagnetic micropulsations. *Journal of Geophysical Research*, *69*(1), 180–181. https://doi.org/10.1029/JZ069i001p00180

James, M. K., Yeoman, T. K., Mager, P. N., & Klimushkin, D. Y. (2016). Multiradar observations of substorm-driven ULF waves. *Journal of Geophysical Research: Space Physics*, *121*(6), 5213–5232. https://doi.org/10.1002/2015JA022102

Jorgensen, A. M., Spence, H. E., Hughes, W. J., & Singer, H. J. (2004). A statistical study of the global structure of the ring current. *Journal of Geophysical Research*, *109*(A12), A12204. https://doi.org/10.1029/2003JA010090

Kale, Z. C., Mann, I. R., Waters, C. L., Goldstein, J., Menk, F. W., & Ozeke, L. G. (2007). Ground magnetometer observation of a cross-phase reversal at a steep plasmapause. *Journal of Geophysical Research*, *112*(A10), A10222. https://doi.org/10.1029/2007JA012367

Kale, Z. C., Mann, I. R., Waters, C. L., Vellante, M., Zhang, T. L., & Honary, F. (2009). Plasmaspheric dynamics resulting from the Hallowe'en 2003 geomagnetic storms. *Journal of Geophysical Research*, *114*(A8), A08204. https://doi.org/10.1029/2009JA014194

Katus, R. M., Gallagher, D. L., Liemohn, M. W., Keesee, A. M., & Sarno-Smith, L. K. (2015). Statistical storm time examination of MLT-dependent plasmapause location derived from IMAGE EUV. *Journal of Geophysical Research: Space Physics*, *120*(7), 5545–5559. https://doi.org/10.1002/2015JA021225

Kepko, L., Spence, H. E., & Singer, H. J. (2002). ULF waves in the solar wind as direct drivers of magnetospheric pulsations. *Geophysical Research Letters*, *29*(8), 391–394. https://doi.org/10.1029/2001GL014405

Kilpua, E. K. J., Hietala, D. L., Koskinen, H. E. J., Pulkkinen, T. I., Rodriguez, J. V., Spence, H. E., et al. (2015). Unraveling the drivers of the storm time radiation belt response. *Geophysical Research Letters*, *42*(9), 3076–3084. https://doi.org/10.1002/2015GL063542

Kim, K.-H., Kim, G.-J., & Kwon, H.-J. (2018). Distribution of equatorial Alfvén velocity in the magnetosphere: A statistical analysis of THEMIS observations. *Earth, Planets and Space*, *70*(1), 174. https://doi.org/10.1186/s40623-018-0947-9

Kistler, L. M., & Mouikis, C. G. (2016). The inner magnetosphere ion composition and local time distribution over a solar cycle. *Journal of Geophysical Research: Space Physics*, *121*(3), 2009–2032. https://doi.org/10.1002/2015JA021883

Kivelson, M. G., & Southwood, D. J. (1986). Coupling of global magnetospheric MHD eigenmodes to field line resonances. *Journal of Geophysical Research*, *91*(A4), 4345–4351. https://doi.org/10.1029/JA091iA04p04345

Kletzing, C. A., Kurth, W. S., Acuna, M., MacDowall, R. J., Torbert, R. B., Averkamp, T., et al. (2013). The Electric and Magnetic Field Instrument Suite and Integrated Science (EMFISIS) on RBSP. *Space Science Reviews*, *179*(1), 127–181. https://doi.org/10.1007/s11214-013-9993-6

Koskinen, H. E. J., & Tanskanen, E. I. (2002). Magnetospheric energy budget and the epsilon parameter. *Journal of Geophysical Research*, *107*(A11), 1415. https://doi.org/10.1029/2002JA009283

Kurth, W. S., De Pascuale, S., Faden, J. B., Kletzing, C. A., Hospodarsky, G. B., Thaller, S., & Wygant, J. R. (2015). Electron densities inferred from plasma wave spectra obtained by the waves instrument on Van Allen Probes. *Journal of Geophysical Research: Space Physics*, *120*(2), 904–914. https://doi.org/10.1002/2014JA020857

Lee, D.-H., Hudson, M. K., Kim, K., Lysak, R. L., & Song, Y. (2002). Compressional mhd wave transport in the magnetosphere 1. Reflection and transmission across the plasmapause. *Journal of Geophysical Research*, *107*(A10), 1307. https://doi.org/10.1029/2002JA009239

Liu, W., Sarris, T. E., Li, X., Elkington, S. R., Ergun, R., Angelopoulos, V., et al. (2009). Electric and magnetic field observations of Pc4 and Pc5 pulsations in the inner magnetosphere: A statistical study. *Journal of Geophysical Research*, *114*(A12), A12206. https://doi.org/10.1029/2009JA014243

Mann, I. R., Wright, A. N., Mills, K. J., & Nakariakov, V. M. (1999). Excitation of magnetospheric waveguide modes by magnetosheath flows. *Journal of Geophysical Research*, *104*(A1), 333–353. https://doi.org/10.1029/1998JA900026

Mauk, B. H., Fox, N. J., Kanekal, S. G., Kessel, R. L., Sibeck, D. G., & Ukhorskiy, A. (2013). Science objectives and rationale for the radiation belt storm probes mission. *Space Science Reviews*, *179*(1), 3–27. https://doi.org/10.1007/s11214-012-9908-y

Murphy, K. R., Mann, I. R., & Sibeck, D. G. (2015). On the dependence of storm time ULF wave power on magnetopause location: Impacts for ULF wave radial diffusion. *Geophysical Research Letters*, *42*(22), 9676–9684. https://doi.org/10.1002/2015GL066592

Nosé, M., Iyemori, T., Nakabe, S., Nagai, T., Matsumoto, H., & Goka, T. (1998). ULF pulsations observed by the ETS-VI satellite: Substorm associated azimuthal Pc 4 pulsations on the nightside. *Earth, Planets and Space*, *50*(1), 63–80. https://doi.org/10.1186/bf03352087

Nosé, M., Iyemori, T., Sugiura, M., & Slavin, J. A. (1995). A strong dawn/dusk asymmetry in Pc5 pulsation occurrence observed by the DE-1 satellite. *Geophysical Research Letters*, *22*(15), 2053–2056. https://doi.org/10.1029/95GL01794

Nykyri, K. (2013). Impact of MHD shock physics on magnetosheath asymmetry and Kelvin-Helmholtz instability. *Journal of Geophysical Research: Space Physics*, *118*(8), 5068–5081. https://doi.org/10.1002/jgra.50499

Ozeke, L. G., Mann, I. R., Murphy, K. R., Jonathan Rae, I., & Milling, D. K. (2014). Analytic expressions for ULF wave radiation belt radial diffusion coefficients. *Journal of Geophysical Research: Space Physics*, *119*(3), 1587–1605. https://doi.org/10.1002/2013JA019204

Pahud, D., Rae, I., Mann, I., Murphy, K., & Amalraj, V. (2009). Ground-based Pc5 ULF wave power: Solar wind speed and MLT dependence. *Journal of Atmospheric and Solar-Terrestrial Physics*, *71*(10), 1082–1092. https://doi.org/10.1016/j.jastp.2008.12.004

Plaschke, F., Glassmeier, K.-H., Sibeck, D. G., Auster, H. U., Constantinescu, O. D., Angelopoulos, V., & Magnes, W. (2009). Magnetopause surface oscillation frequencies at different solar wind conditions. *Annales Geophysicae*, *27*(12), 4521–4532. https://doi.org/10.5194/angeo-27-4521-2009

Posch, J. L., Engebretson, M. J., Pilipenko, V. A., Hughes, W. J., Russell, C. T., & Lanzerotti, L. J. (2003). Characterizing the long-period ulf response to magnetic storms. *Journal of Geophysical Research*, *108*(A1), 1029. https://doi.org/10.1029/2002JA009386

Rae, I. J., Donovan, E. F., Mann, I. R., Fenrich, F. R., Watt, C. E. J., Milling, D. K., et al. (2005). Evolution and characteristics of global Pc5 ULF waves during a high solar wind speed interval. *Journal of Geophysical Research*, *110*(A12), A12211. https://doi.org/10.1029/2005JA011007

Rae, I. J., Murphy, K. R., Watt, C. E., Sandhu, J. K., Georgiou, M., Degeling, A. W., et al. (2019). How do ultra-low frequency waves access the inner magnetosphere during geomagnetic storms? *Geophysical Research Letters*, *46*(19), 10699–10709. https://doi.org/10.1029/2019GL082395

Raymer, K. M. (2018). Influences on the location of the Earth's magnetopause (Doctoral dissertation). Retrieved from https://leicester.figshare.com/articles/thesis/Influences_on_the_location_of_the_Earth_s_magnetopause/10222037

Sandhu, J. K., Rae, I. J., & Walach, M.-T. (2021). Challenging the use of ring current indices during geomagnetic storms. *Journal of Geophysical Research: Space Physics*, *126*(2), e2020JA028423. https://doi.org/10.1029/2020JA028423

Sandhu, J. K., Rae, I. J., Wygant, J. R., Breneman, A. W., Tian, S., Watt, C. E. J., et al. (2021). ULF wave driven radial diffusion during geomagnetic storms: A statistical analysis of Van Allen Probes observations. *Journal of Geophysical Research: Space Physics*, *126*(4), e2020JA029024. https://doi.org/10.1029/2020JA029024

Sandhu, J. K., Yeoman, T. K., & Rae, I. J. (2018). Variations of field line eigenfrequencies with ring current intensity. *Journal of Geophysical Research: Space Physics*, *123*(11), 9325–9339. https://doi.org/10.1029/2018JA025751

Sandhu, J. K., Yeoman, T. K., Rae, I. J., Fear, R. C., & Dandouras, I. (2017). The dependence of magnetospheric plasma mass loading on geomagnetic activity using cluster. *Journal of Geophysical Research: Space Physics*, *122*(9), 9371–9395. https://doi.org/10.1002/2017JA024171

Shue, J.-H., Song, P., Russell, C. T., Steinberg, J. T., Chao, J. K., Zastenker, G., et al. (1998). Magnetopause location under extreme solar wind conditions. *Journal of Geophysical Research*, *103*(A8), 17691–17700. https://doi.org/10.1029/98JA01103

Simms, L. E., Pilipenko, V. A., & Engebretson, M. J. (2010). Determining the key drivers of magnetospheric Pc5 wave power. *Journal of Geophysical Research*, *115*(A10), A10241. https://doi.org/10.1029/2009JA015025

Southwood, D. (1974). Some features of field line resonances in the magnetosphere. *Planetary and Space Science*, *22*(3), 483–491. https://doi.org/10.1016/0032-0633(74)90078-6

Spasojević, M., Goldstein, J., Carpenter, D. L., Inan, U. S., Sandel, B. R., Moldwin, M. B., & Reinisch, B. W. (2003). Global response of the plasmasphere to a geomagnetic disturbance. *Journal of Geophysical Research*, *108*(A9), 1340. https://doi.org/10.1029/2003JA009987

Spearman, C. (1987). The proof and measurement of association between two things. *The American Journal of Psychology*, *100*(3/4), 441–471. https://doi.org/10.2307/1422689

Staples, F. A., Rae, I. J., Forsyth, C., Smith, A. R. A., Murphy, K. R., Raymer, K. M., et al. (2020). Do statistical models capture the dynamics of the magnetopause during sudden magnetospheric compressions? *Journal of Geophysical Research: Space Physics*, *125*(4), e2019JA027289. https://doi.org/10.1029/2019JA027289

Takahashi, K., Lee, D.-H., Merkin, V. G., Lyon, J. G., & Hartinger, M. D. (2016). On the origin of the dawn-dusk asymmetry of toroidal Pc5 waves. *Journal of Geophysical Research: Space Physics*, *121*(10), 9632–9650. https://doi.org/10.1002/2016JA023009

Takahashi, K., Sato, N., Warnecke, J., Lühr, H., Spence, H. E., & Tonegawa, Y. (1992). On the standing wave mode of giant pulsations. *Journal of Geophysical Research*, *97*(A7), 10717–10732. https://doi.org/10.1029/92JA00382

Takahashi, K., Yumoto, K., Claudepierre, S. G., Sanchez, E. R., Troshichev, O. A., & Janzhura, A. S. (2012). Dependence of the amplitude of Pc5-band magnetic field variations on the solar wind and solar activity. *Journal of Geophysical Research*, *117*(A4), A04207. https://doi.org/10.1029/2011JA017120

Thompson, R. L., Morley, S., Watt, C., Bentley, S., & Williams, P. (2019). Pro-L* - A Probabilistic L* Mapping Tool for Ground Observations to the Magnetic Equator. In AGU Fall meeting abstracts (Vol. 2019, p. SM41C-3245).

Torrence, C., & Compo, G. P. (1998). A practical guide to wavelet analysis. *Bulletin of the American Meteorological Society*, *79*(1), 61–78. https://doi.org/10.1175/1520-0477(1998)079<0061:apgtwa>2.0.co;2

Usanova, M. E., Darrouzet, F., Mann, I. R., & Bortnik, J. (2013). Statistical analysis of emic waves in plasmaspheric plumes from cluster observations. *Journal of Geophysical Research: Space Physics*, *118*(8), 4946–4951. https://doi.org/10.1002/jgra.50464

Walach, M.-T., & Grocott, A. (2019). SuperDARN observations during geomagnetic storms, geomagnetically active times, and enhanced solar wind driving. *Journal of Geophysical Research: Space Physics*, *124*, 5828–5847. https://doi.org/10.1029/2019JA026816

Wharton, S. J., Rae, I. J., Sandhu, J. K., Walach, M.-T., Wright, D. M., & Yeoman, T. K. (2020). The changing eigenfrequency continuum during geomagnetic storms: Implications for plasma mass dynamics and ULF wave couping. *Journal of Geophysical Research: Space Physics*, *125*, e2019JA027648. https://doi.org/10.1029/2019JA027648

Woch, J., Kremser, G., & Korth, A. (1990). A comprehensive investigation of compressional ULF waves observed in the ring current. *Journal of Geophysical Research*, *95*(A9), 15113–15132. https://doi.org/10.1029/JA095iA09p15113

Yue, C., Bortnik, J., Li, W., Ma, Q., Wang, C.-P., Thorne, R. M., et al. (2019). Oxygen ion dynamics in the earth's ring current: Van Allen Probes observations. *Journal of Geophysical Research: Space Physics*, *124*(10), 7786–7798. https://doi.org/10.1029/2019JA026801

Zong, Q.-G., Zhou, X.-Z., Wang, Y. F., Li, X., Song, P., Baker, D. N., et al. (2009). Energetic electron response to ULF waves induced by interplanetary shocks in the outer radiation belt. *Journal of Geophysical Research: Space Physics*, *114*(A10), A10204. https://doi.org/10.1029/2009JA014393